NANO · MICRO
small
www.small-journal.com

Check for updates

Atomic Layer Deposition of Textured $Li_4Ti_5O_{12}$: A High-Power and Long-Cycle Life Anode for Lithium-Ion Thin-Film Batteries

Jan Speulmanns, Alireza M. Kia, Sascha Bönhardt, Wenke Weinreich, and Philipp Adelhelm*

The "zero-strain" $Li_4Ti_5O_{12}$ is an attractive anode material for 3D solid-state thin-film batteries (TFB) to power upcoming autonomous sensor systems. Herein, $Li_4Ti_5O_{12}$ thin films fabricated by atomic layer deposition (ALD) are electrochemically evaluated for the first time. The developed ALD process with a growth per cycle of 0.6 Å cycle^{-1} at 300 °C enables high-quality and dense spinel films with superior adhesion after annealing. The short lithium-ion diffusion pathways of the nanostructured 30 nm films result in excellent electrochemical properties. Planar films reveal 98% of the theoretical capacity with 588 mAh cm^{-3} at 1 C. Substrate-dependent film texture is identified as a key tuning parameter for exceptional C-rate performance. The highly parallel grains of a strong out-of-plane (111)-texture allow capacities of 278 mAh cm^{-3} at extreme rates of 200 C. Outstanding cycle performance is demonstrated, resulting in 97.9% capacity retention of the initial 366 mAh cm^{-3} after 1000 cycles at 100 C. Compared to other deposition techniques, the superior performance of ALD $Li_4Ti_5O_{12}$ is a breakthrough towards scalable high-power 3D TFBs.

1. Introduction

The ongoing enhancement of miniaturization and energy-efficiency of electronic devices enabled a tremendous increase in ultralow-power Internet-of-Thing (IoT) devices.[1] In the upcoming years, the market for applications such as autonomous sensors, wearable devices, and medical implants will grow up to 100 billion USD.[1,2] The shrinking device sizes of portable electronics require microsized on-chip energy storage solutions with high-energy and high-power capability. These demands are beyond the abilities of liquid lithium (Li)-ion batteries due to limited miniaturization potential and inherent risks of the liquid electrolyte such as flammability and leakage.

TFBs with solid-state electrolytes and binder-free electrodes are a promising alternative. In general, interfaces are more pronounced in thin-film devices, which remains challenging in all-solid-state batteries.[3] TFBs provide high-power density, long cycle life, low self-discharge, high-temperature and chemical stability, on-chip integration, and miniaturization.[4] These properties pave the way for future replacement of standard on-chip supercapacitors.[5] However, the small form factor and short Li diffusion length of TFBs come at the cost of low energy density. So-called 3D TFBs can partially compensate this by increasing energy density per footprint area. Thereby the battery layer stack is coated over a microstructured substrate with an enhanced surface area.[6] A first functional full cell 3D TFB was recently demonstrated by Pearse et al.[7] Moitzheim et al. reported an extensive overview of the current state, challenges, and outlooks of 3D TFBs.[8]

ALD is the ideal technique enabling the required conformal, pinhole-free deposition and stoichiometric control of nanometer-thin films on highly structured surfaces. The vapor-phase technique based on sequential, self-limiting surface reactions is well understood and an industrial standard in integrated circuit manufacturing.[9] However, the deposition of Li metal is not possible and Li compounds remain challenging.[10,11] Functional ALD films of cathode materials such as $LiMn_2O_4$[12] or $LiCoO_2$[13] and solid-state electrolytes such as LiPON[14] or $Li_xAl_ySi_zO$[15] were demonstrated. However, Li-containing anode materials directly fabricated by ALD were not yet electrochemically evaluated. Only closely related ALD TiO_2 anodes were successfully investigated and optimized.[16,17]

Spinel $Li_4Ti_5O_{12}$ (LTO) is a well-suited anode for 3D TFBs. The material undergoes a phase transition to the rocksalt-like structure during lithiation by rearranging the Li atoms with minimal volume change below 0.1%.[18] This so-called "zero-strain"

J. Speulmanns, A. M. Kia, S. Bönhardt, Dr. W. Weinreich
Center Nanoelectronic Technologies
Fraunhofer Institute for Photonic Microsystems
An der Bartlake 5, 01109 Dresden, Germany
E-mail: jan.speulmanns@ipms.fraunhofer.de

J. Speulmanns, Prof. P. Adelhelm
Department of Chemistry
Humboldt-University Berlin
Brook-Taylor-Strasse 2, 12489 Berlin, Germany

Prof. P. Adelhelm
Helmholtz-Zentrum Berlin für Materialien und Energie
Hahn-Meitner-Platz 1, 14109 Berlin, Germany

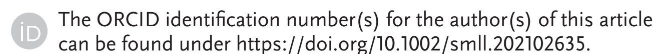
The ORCID identification number(s) for the author(s) of this article can be found under https://doi.org/10.1002/smll.202102635.

© 2021 The Authors. Small published by Wiley-VCH GmbH. This is an open access article under the terms of the Creative Commons Attribution-NonCommercial License, which permits use, distribution and reproduction in any medium, provided the original work is properly cited and is not used for commercial purposes.

DOI: 10.1002/smll.202102635

behavior inhibits delamination or additional stress of the film in the high-aspect structures. Furthermore, it enables a high Li-ion insertion/extraction reversibility and thus long cycle life.[19,20] The 3D Li diffusion pathways of $Li_4Ti_5O_{12}$ enable a high degree of freedom for diffusion, not only perpendicular to the substrate.[21] Another advantage is the superior safety with a stable lithium insertion/extraction voltage at 1.55 V versus Li^+/Li compared to Li metal batteries.[22] Up to three Li ions per formula unit can be intercalated during lithiation in the potential range of 1 to 2.5 V versus Li^+/Li forming $Li_7Ti_5O_{12}$. Limitations of $Li_4Ti_5O_{12}$ are the moderate theoretical capacity of 175 mAh g^{-1} or 600 mAh cm^{-3} and low electronic and ionic conductivity of its end members.[22,23] Recently, Wang et al. revealed that the counterintuitive excellent high-rate performance could be explained by the facile Li-ion transport mediated by metastable intermediates, with low transport energy barriers.[24] Several strategies have been investigated compensating the poor intrinsic material properties such as surface modification, doping, grain growth control, or nanostructuring.[22,23,25] For example, the benefit of shorter diffusion pathways for improved C-rate performance is shown for sputtered thin films.[26,27] Besides, thin films can be utilized as model systems for large-scale solid-state batteries to understand nanoionic or interface effects.[28]

In general, physical vapor deposition (PVD)-based processes are not suitable for conformal coating of structured substrates. As described earlier, ALD is the ideal technique for the fabrication of 3D TFBs. The principle feasibility of classic supercycle ALD for the fabrication of $Li_xTi_yO_z$ was proven several years ago.[29,30] Depending on the precursor combination, the films were rather air-sensitive and with low Li concentration.[29] The utilization of lithium-*tert*-butoxide (LTB) and titanium tetraisopropoxide ($Ti(O^iPr)_4$) leads to controlled Li contents over a wide range and stable spinel films.[30,31] Recently, Bönhardt et al. demonstrated a novel three-step ALD process with LTB and tetrakis (dimethylamino) titanium (TDMAT), achieving spinel $Li_4Ti_5O_{12}$ with ideal stoichiometry and highly conformal coating.[32] However, $Li_4Ti_5O_{12}$ films by ALD have not yet been electrochemically investigated.

In this study, we systematically evaluate the film texture of nanostructured ALD $Li_4Ti_5O_{12}$ as a tuning parameter for electrochemical performance. To the best of the authors' knowledge, this is the first time ALD $Li_4Ti_5O_{12}$ films have been electrochemically probed. A three-step ALD process with a lithium hexamethyldisilazide (LiHMDS) precursor is successfully developed, resulting in high-quality spinel $Li_4Ti_5O_{12}$. The influence of the substrate on the crystallization behavior and film texture is investigated. The highly parallel grains of a film with a strongly preferred growth direction appear beneficial for Li-ion transport. Thus, ALD $Li_4Ti_5O_{12}$ films with a strong (111)-texture offer excellent high-rate performance with ultralong cycle life.

2. Results and Discussion

2.1. ALD Process Development of $Li_4Ti_5O_{12}$

A three-step ALD process with LiHMDS, TDMAT, and water (H_2O) fabricating spinel $Li_4Ti_5O_{12}$ was successfully developed. During process development, the LiHMDS pulse time was varied, and all other parameters were kept constant. The thickness of the dense, homogenous, and crack-free films on the SiO_2 substrates was verified by scanning electron microscopy (SEM) and in-situ spectroscopic ellipsometry (iSE). **Figure 1a** shows the growth per cycle (GPC) by SEM with an error of 0.03 Å $cycle^{-1}$ for various pulse times of LiHMDS for the deposition with 500 cycles. Three deposition regimes are visible depending on the LiHMDS pulse time. In regime I, a GPC of 0.44 Å $cycle^{-1}$ is reached for the formation of TiO_2 without the addition of LiHMDS. After an initial drop with the beginning incorporation of Li in regime II, the GPC increases from 0.34 to 0.6 Å $cycle^{-1}$ for pulse times of 2 to 5 s. The GPC values measured via iSE, visualized by downward triangles, match with the SEM data. At 5 s a small GPC plateau is visible. However, the GPC strongly increases to around 1 Å $cycle^{-1}$ for longer pulse times in regime III. This indicates a more chemical vapor deposition (CVD)-like deposition due to precursor decomposition for pulse times above 5 s.

Grazing incidence X-ray diffraction (GI-XRD) was conducted, obtaining phase information for further investigation of the process regimes. All films were amorphous after the deposition. 2θ diffractograms of the polycrystalline films after rapid thermal processing (RTP) annealing at 700 °C for 30 s are shown in Figure 1b. The expected formation of TiO_2, without a LiHMDS pulse, is visible in Regime I. In Regime II, with pulse times of 2 to 5 s, the peaks match spinel $Li_4Ti_5O_{12}$ (PDF 00-049-0207) with a cubic crystal system and Fd-3m spacegroup. These $Li_4Ti_5O_{12}$ films did not reveal phase impurities. However, small quantities of impurities cannot be excluded. The strong increase of the height of the LTO (111) reflex around 18.33° with longer pulse times is shown in Figure S1a in the Supporting Information. This cannot only be explained by the difference in film thickness but also indicates a stronger preferred growth direction. In general, the (111) reflex is the most pronounced for spinel $Li_4Ti_5O_{12}$. The film with 2 s pulse time has a visible LTO (400) reflex around 43.2°, whereas it is vanished for all other films. This indicates a highly out-of-plane (111)-textured $Li_4Ti_5O_{12}$ film for a LiHMDS pulse time of 5 s. In regime III, the diffraction patterns show additional peaks indicating phase impurities. The peaks match either Li_2SiO_3 (PDF 00-029-0828) or $Li_2Si_2O_5$ (PDF 00-014-0322). The incorporation of Si in the film originates from the LiHMDS precursor, which contains two Si per Li. The present formation of $Li_xSi_yO_z$ for LiHMDS pulse times above 5 s could be due to precursor decomposition or unreacted ligands of the physisorbed LiHMDS. The Si incorporation in the film could be precisely controlled by the utilization of plasma-enhanced ALD.[33] However, this mechanism is an undesired side reaction for the here applied thermal ALD. The increased amount of incorporated Si in the deposited film could explain the higher GPCs in process regime III.

The optimized ALD process with a 5 s LiHMDS pulse for the fabrication of polycrystalline spinel $Li_4Ti_5O_{12}$ is in good agreement with an earlier study following the same ALD three-step procedure.[32] There LTB was used as a Li precursor instead of LiHMDS. Films deposited with both precursors reveal a strong (111)-textured $Li_4Ti_5O_{12}$ film on SiO_2 after annealing. Other reported classic supercycle ALD processes of $Li_xTi_yO_z$ lead to films with either (400)-texture on platin or weak (111)-texture

© 2021 The Authors. Small published by Wiley-VCH GmbH

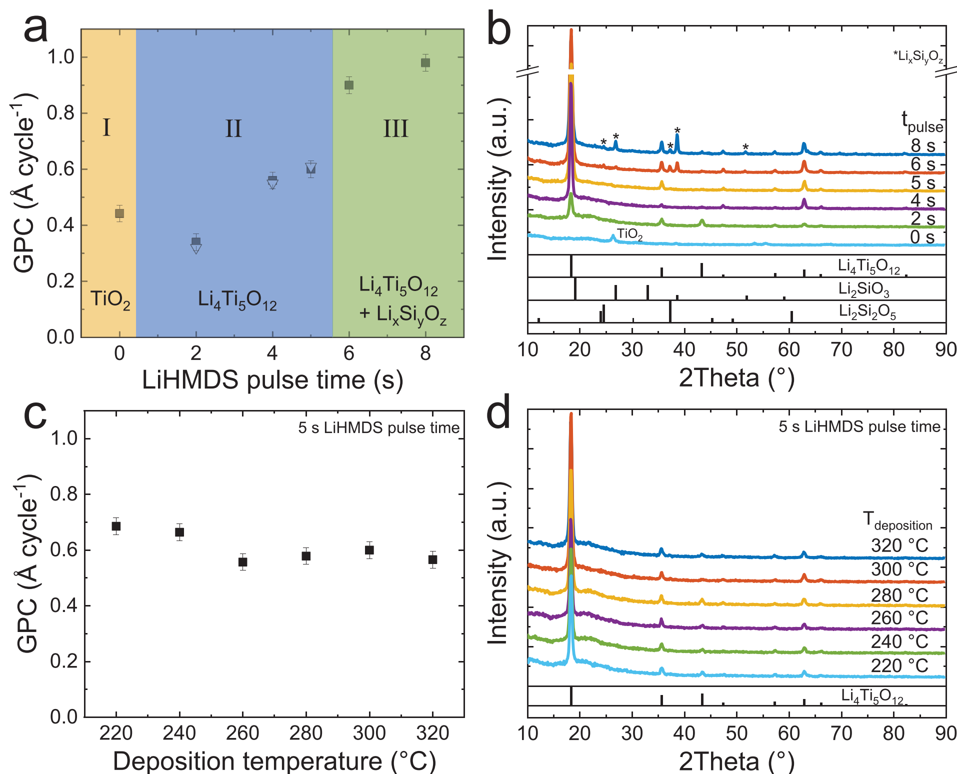

Figure 1. $Li_4Ti_5O_{12}$ ALD process development at 300 °C with LiHMDS pulse time-dependent a) growth per cycle (GPC) measured via SEM (squares) and iSE (downward triangles) and b) GI-XRD diffractograms with interrupted Y-axis. Pattern comparison performed with $Li_4Ti_5O_{12}$ (PDF 00-049-0207), Li_2SiO_3 (PDF 00-029-0828), and $Li_2Si_2O_5$ (PDF 00-014-0322). Deposition temperature-dependent c) GPC and d) GI-XRD diffractograms with a constant 5 s LiHMDS pulse time.

on nitrogen-doped carbon nanotubes.[29,30] Furthermore, issues with the control of stoichiometry and longtime stability occurred. In general, a pronounced (111)-texture is typical for polycrystalline sputtered[26] and can be selected for epitaxial[25,34] $Li_4Ti_5O_{12}$ thin films.

Next, the ALD temperature window was investigated with a constant 5 s LiHMDS pulse and variation of the deposition temperature between 220 and 320 °C. Figure 1c demonstrates that the ALD process is stable over the whole temperature range with a GPC variation between 0.56 and 0.69 Å cycle^{-1}. The slightly elevated GPCs below 250 °C could be related to a propagated formation of lithium hydroxide (LiOH) at lower temperatures.[35] The 2θ diffractograms show the formation of phase-pure spinel $Li_4Ti_5O_{12}$ for all deposition temperatures. Figure S1b in the Supporting Information illustrates that the height of the LTO (111) reflex is the highest for 300 °C. 280 and 320 °C show similar but lower values. The remaining deposition temperatures are all on the same level at around 60% of the maximum height. All deposition temperatures lead to a preferred (111) growth direction. The (400) reflex is suppressed only for 300 °C. However, for the other deposition temperatures, the intensity of the (400) peak is minimal compared to the (111) peak. For electrochemical characterization, film deposition will be performed with 5 s LiHMDS pulse time at 300 °C with 500 cycles leading to 30 nm films of spinel $Li_4Ti_5O_{12}$ after annealing.

2.2. Crystallization Effect on the Electrochemical Behavior of $Li_4Ti_5O_{12}$

For electrochemical measurements, the $Li_4Ti_5O_{12}$ thin film has to be deposited on a current collector. Furthermore, the utilization of Si wafers as underlying substrate requires a Li-ion diffusion barrier to suppress capacity loss and device detachment due to the expansion of the Si substrate upon undesired lithiation.[36,37] In an earlier study, we proved that ultrathin 10 nm ALD and 35 nm pulsed CVD (pCVD) TiN films are excellent bifunctional current collectors and diffusion barriers.[36] Hence, further development was performed with these TiN films coated on highly-doped p-type Si (100) wafers. The influence of the crystalline TiN films on the crystallization of $Li_4Ti_5O_{12}$ will be investigated next.

The crystallization behavior of $Li_4Ti_5O_{12}$ films with 5 s LiHMDS pulse time on both TiN substrates and exemplary, the consequential electrochemical behavior on ALD TiN are illustrated in **Figure 2**. Figure 2a,b shows the peak height of the LTO (111) reflex upon different annealing times at 750 °C on both TiN substrates. In contrast to the amorphous SiO_2 substrate, no peak is visible for 30 s annealing of $Li_4Ti_5O_{12}$ on ALD TiN. The peak height and thus the crystallization degree increase from 3 to 8 min. For 11 min further crystallization is not visible. Hence, it can be concluded that 8 min is sufficient for complete crystallization with the utilized annealing setup. Figure 2b

© 2021 The Authors. Small published by Wiley-VCH GmbH

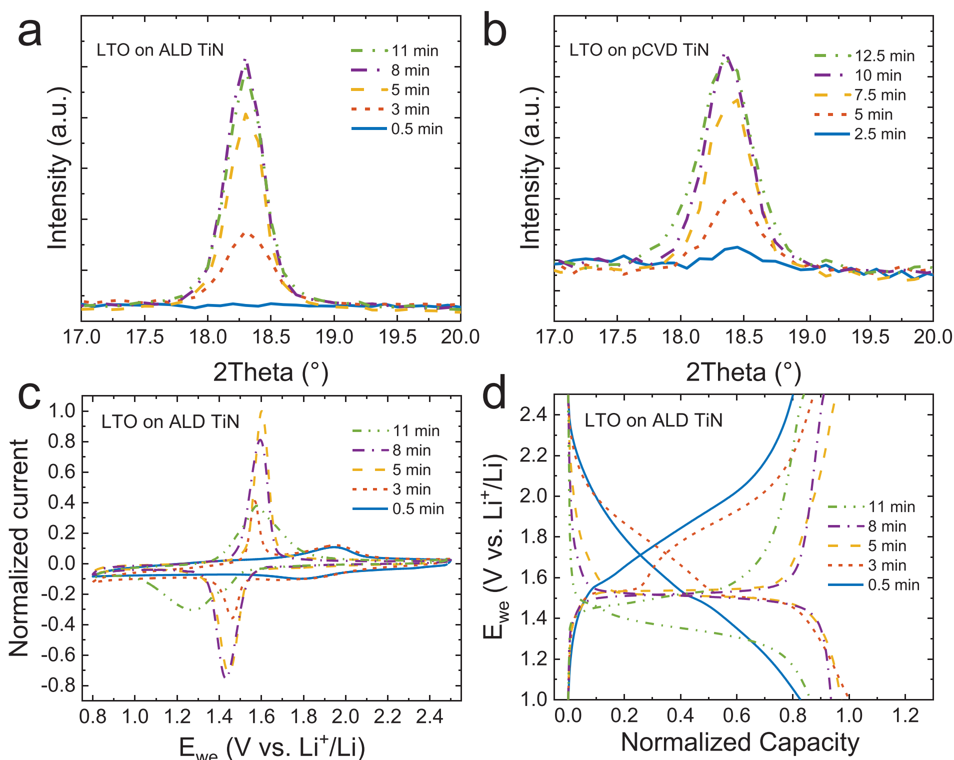

Figure 2. Time-dependent crystallization behavior of the LTO (111) reflex on a) 10 nm ALD TiN and b) 35 nm pCVD TiN at 750 °C via RTP. Effect of the crystallization degree on the electrochemical properties in c) CV at 0.5 mV s^{-1} and d) the second Galvanostatic cycle at 1 C.

illustrates the same behavior for the pCVD TiN substrate with overall higher annealing times and an optimum time of 10 min. 15 to 20 times longer annealing times are required on TiN substrates for complete crystallization at 750 °C compared to SiO_2 substrates at 700 °C. The annealing temperature of 750 °C was chosen since 700 °C lead to even longer annealing times, and at 800 °C film delamination occurred. The inhibited crystal growth on TiN could be due to the characteristics of the interface and the mismatch of thermal expansion coefficients. In general, the interface properties strongly influence the nucleation behavior, such as heterogeneous and homogeneous nucleation, and crystallization kinetics in thin films.[38–41] The surfaces of the amorphous SiO_2 and polycrystalline TiN substrates have different characteristics such as surface energy, termination chemistry, roughness, and local structure.[36,38,41] However, the nucleation behavior of $Li_4Ti_5O_{12}$ thin films was not yet explained in literature. Kia et al. found that the crystalline phase of closely related TiO_2 ALD thin films is influenced by SiO_2 or TiN substrates upon annealing by favoring different nucleation mechanisms.[38] The significant influence of the interface energy on crystallization temperature is typical for ALD thin films, but not fully understood.[41] The 50% larger thermal expansion coefficient of $Li_4Ti_5O_{12}$ with 15.6×10^{-6} K^{-1} compared to TiN with 10.3×10^{-6} K^{-1} could also hamper crystallization.[42] The mismatch of thermal expansion between the thin film and the underlying substrate could result in residual stress and changes of the local mechanical stress field in the thin film.[39,43] In general, film stress is a factor that can significantly affect the crystallization temperature and kinetics of thin films.[44] The difference in annealing time between both TiN substrates could be due to the difference in film thickness, the dissimilar TiN texture and subsequent various lattice mismatches, the higher surface roughness of the pCVD film, and a higher content of titanium oxynitride ($Ti_xO_yN_z$) at the surface of the pCVD film.[36]

The electrochemical behavior is directly correlated to the crystallization degree of the $Li_4Ti_5O_{12}$ films.[45–47] Here, we want to explore the optimum annealing time for electrochemical performance and the origin of the non-plateau capacity in galvanostatic measurements. Figure 2c shows the cyclic voltammetry (CV) measurement at 0.5 mV s^{-1} of the various annealing times exemplary for the ALD TiN substrate. The current is normalized to the maximum current of all samples for easier comparison. 0.5 min does not show the typical $Li_4Ti_5O_{12}$ peaks around 1.55 V versus Li^+/Li, but broad redox behavior around 1.81 and 1.95 V versus Li^+/Li for lithiation and delithiation, respectively. These peaks do not correlate with TiO_2 impurities and could be accounted for the still amorphous $Li_4Ti_5O_{12}$ film.[45] For 3 min, peaks at 1.46 (lithiation) and 1.57 V versus Li^+/Li (delithiation) start to evolve, indicating crystalline $Li_4Ti_5O_{12}$. The broad amorphous contribution remains unmodified. Further crystallization until 8 min leads to increased $Li_4Ti_5O_{12}$ related peaks and vanishing of the amorphous peaks. 5 min shows a sharper and more pronounced peak during delithiation. Although 11 min gave a similar XRD signature as 8 min, the electrochemical behavior differs significantly. The delithiation peak is at the same position, however strongly suppressed and broadened. A shift of the lithiation peak to a lower potential of 1.27 V versus Li^+/Li is visible, indicating higher

© 2021 The Authors. Small published by Wiley-VCH GmbH

internal resistance. The CV measurements indicate that 8 min is the optimum annealing time.

A closer investigation was done by galvanostatic cycling with potential limits (GCPL) at 1 C in the potential range of 1 to 2.5 V versus Li^+/Li. The length of the potential plateaus of $Li_4Ti_5O_{12}$ around 1.55 V versus Li^+/Li correlates with the crystallization degree. Figure 2d demonstrates a high consistency of the GCPL and the CV measurements. The capacity values were normalized to the obtained maximum capacity of all samples. No plateau voltage is visible for 0.5 min annealing. Similar to the CV result, 3 min shows small plateaus around 1.55 V versus Li^+/Li, and the remaining capacity of over 70% is related to the tails of the curve. 5 and 8 min both show large plateau areas around 1.52 and 1.56 V versus Li^+/Li for lithiation and delithiation, respectively. However, for 5 min the tails are more pronounced and less steep. Overall, the increase in LTO crystallinity leads to a more defined redox behavior reflected by a sharpening of the CV profiles and more distinct plateaus in the GCPL measurements. The optimum (largest plateau capacity) is reached for a crystallization time of 8 min. Further annealing leads to a reduced capacity, smeared out plateaus, and shifting of the open-circuit voltage to lower potentials. Possible explanations could be the formation of blocking surface species due to Li loss, film delamination inhibiting electrical contact to the substrate, or larger grains increasing resistance due to the poor conductivity of $Li_4Ti_5O_{12}$. The GCPL measurements confirm that the completely crystallized film at 8 min results in the best electrochemical performance. It should be noted that the crystallization degree-dependent electrochemical behavior of $Li_4Ti_5O_{12}$ is analogous on the pCVD TiN substrate, with an optimum GCPL voltage profile for 10 min annealing time.

The tails above and below the voltage plateaus can be assigned to amorphous and surface contributions.[25,45,47] Full crystallization on ALD TiN at 8 min results in the largest plateau voltage and steepest tails towards the potential limits. This demonstrates that amorphous material primarily added to the initial tail capacities. The remaining minimized non-plateau capacity could be accounted as a surface capacity contribution.[25] Cunha et al. showed that bulk to surface contribution can be sufficiently separated by only considering the plateau between 1.5 to 1.6 V versus Li^+/Li. In general, nanostructured $Li_4Ti_5O_{12}$ thin films show a higher contribution of surface capacity due to a lower bulk to surface ratio.[48] Here, the bulk capacity ratio is rather large for 30 nm $Li_4Ti_5O_{12}$ on ALD TiN with around 85% compared to around 50% for epitaxial 55 nm $Li_4Ti_5O_{12}$ films.[25] The ratio of the presented ALD film is in agreement with a simulated voltage profile for 30 nm particles by Ganapathy et al.[48] Hirayama et al. probed 20 nm epitaxial $Li_4Ti_5O_{12}$ films exhibiting around 55% bulk capacity.[49] In the next section, we will discuss the influence of the texture of $Li_4Ti_5O_{12}$ films on the electrochemical performance and the mechanism of the surface capacity.

2.3. Film Texture Influence on $Li_4Ti_5O_{12}$ Performance

The orientation and primarily the surface crystal facets significantly affect the stored capacity and the voltage profile for epitaxial, i.e., single crystalline, $Li_4Ti_5O_{12}$ thin films.[25,49] Here, we will investigate if polycrystalline textured $Li_4Ti_5O_{12}$ thin films reveal a similar dependency.

Figure 3 illustrates that the $Li_4Ti_5O_{12}$ out-of-plane texture depends on the underlying TiN substrate. Both $Li_4Ti_5O_{12}$ samples were annealed at the optimum conditions of 8 and 10 min on ALD and pCVD TiN, respectively, discovered in the previous section. In a previous study, we showed that ALD TiN has a slight (111)-texture, whereas pCVD TiN revealed a strong (200) preferred growth direction.[36] Figure 3a shows a clear difference in the 2θ diffractograms of $Li_4Ti_5O_{12}$ on both TiN substrates. It should be noted that the reflexes match well with the reference patterns for spinel $Li_4Ti_5O_{12}$ and TiN. However, a small quantity of TiO_2 impurities is visible for both samples. This could indicate a minor Li loss due to the significantly longer annealing times compared to the SiO_2 substrate samples. The most apparent difference is visible for the LTO (111) reflex around 18.33°, see Figure S2 in the Supporting Information. The intensity on the pCVD TiN substrate is one order of magnitude lower. The high-resolution 2θ diffractogram from 34° to 46° with a smaller step size of 0.01° to distinguish the LTO (400) reflex is displayed in Figure 3b. It should be noted that the signal of the ALD TiN substrate was magnified by a factor of two for improved visibility. The LTO (400) reflex is distinguishable from the TiN (200) reflex for the pCVD TiN substrate due to the high resolution. However, the (400) reflex is almost vanished for the $Li_4Ti_5O_{12}$ film on ALD TiN. Comparing the peak heights of LTO (111) and (400) reflexes can give information of a preferred growth direction. The ratios are 48 and 0.9 for the ALD TiN and pCVD TiN substrates, respectively. The ratio for the reference (PDF 00-049-0207) is 1.6. Hence, it can be stated that texture follows the preferred growth direction of the TiN substrates. This results in a strong (111)-texture for $Li_4Ti_5O_{12}$ on ALD TiN and a slight (400)-texture on pCVD TiN. The high-resolution 2θ diffractogram in Figure S2 in the Supporting Information reveals the peak positions of the LTO (111) reflexes on the various substrates. The peak positions are similar with 18.34° on SiO_2 and ALD TiN. The peak shifted to a higher value of 18.36° for the pCVD TiN substrate. According to Bragg's law and the cubic lattice system, this could imply a smaller lattice constant resulting in compressed grains. Compressive strain is attributed to a higher Li-ion diffusion energy barrier and consequential slower transport for $Li_4Ti_5O_{12}$.[27] The tilted SEM micrographs in Figure 3c,d show that the $Li_4Ti_5O_{12}$ films on both TiN substrates are closed, dense, and without microcracks allowing excellent contact to the current collector and in between the grains. The surfaces of the $Li_4Ti_5O_{12}$ films show similar roughness. However, the (400)-textured $Li_4Ti_5O_{12}$ is expected to have slightly rougher surface features due to the higher surface roughness of the underlying pCVD TiN film.[36] Figure S3 in the Supporting Information shows the cross-section micrographs of both samples, demonstrating a good agreement of the measured film thicknesses with the aimed thickness of 30 nm. We show that the preferred growth direction of the polycrystalline $Li_4Ti_5O_{12}$ films by ALD strongly depends on the substrate type leading to a strong (111)-texture on ALD TiN and slight (400)-texture on pCVD TiN. From now on, the $Li_4Ti_5O_{12}$ samples on ALD TiN and on pCVD TiN will be referred to as LTO (111) and LTO (400), respectively.

© 2021 The Authors. Small published by Wiley-VCH GmbH

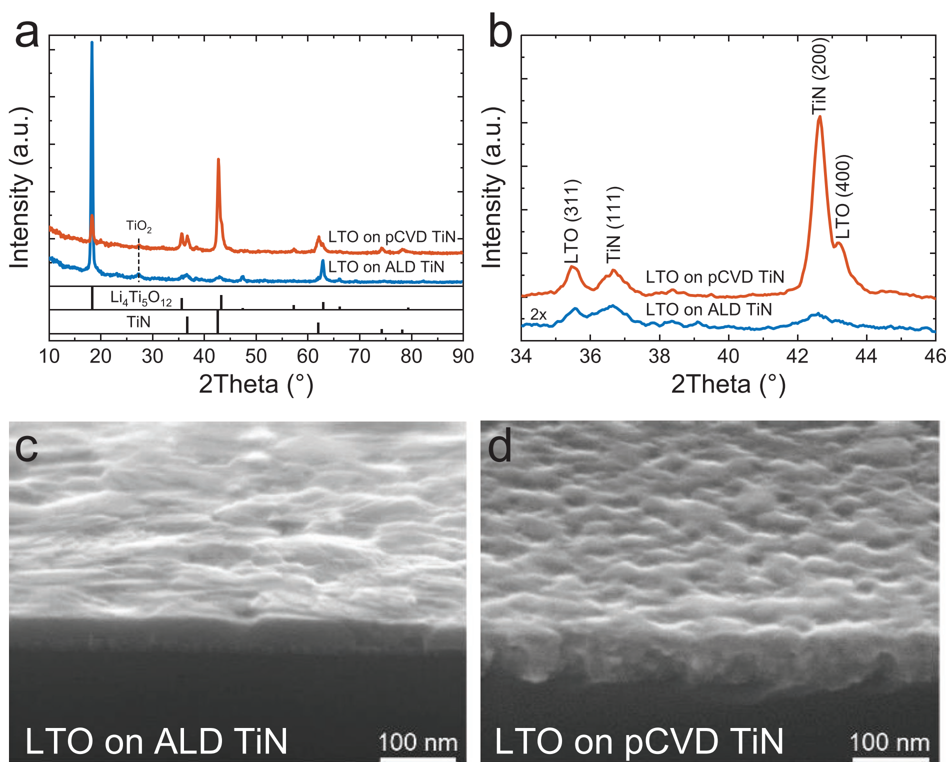

Figure 3. The comparison of a) an overview (10–90°) and b) high-resolution (34–46°) GI-XRD diffractograms of fully crystallized $Li_4Ti_5O_{12}$ on the different TiN substrates. The referenced reflexes were extracted from PDF 00-049-0207 and PDF 00-038-1420. Tilted SEM micrographs of $Li_4Ti_5O_{12}$ on c) 10 nm ALD TiN and d) 35 nm pCVD TiN.

Figure 4 demonstrates that the texture of the 30 nm $Li_4Ti_5O_{12}$ films has an apparent effect on the electrochemical behavior, especially for high C-rates. The CV measurements at 0.5 mV s^{-1} between 1 and 2.5 V versus Li^+/Li with current densities normalized to the surface area are shown in Figure 4a. Both show similar behavior with strong and clear $Li_4Ti_5O_{12}$ related redox pairs. However, LTO (400) has slightly broader peaks with smaller peak current densities and higher potential separation. LTO (111) reveals lithiation and delithiation peaks at 1.46 and 1.57 V versus Li^+/Li, respectively. For LTO (400), the positions are at 1.44 and 1.58 V versus Li^+/Li. Overall, the non-peak current densities are larger for LTO (400), especially towards the potential limits. GCPL at 1 C reveals a similar behavior in Figure 4b. It should be noted that both 30 nm films revealed excellent capacities close to the theoretical capacity (C_{th}) of 600 mAh cm^{-3} with 588 and 575 mAh cm^{-3} for (111)- and (400)-textures, respectively. The plateau potentials match well, although LTO (111) shows more distinct plateaus. The flat voltage areas for LTO (111) are located around 1.51 and 1.53 V versus Li^+/Li compared to 1.50 and 1.53 V versus Li^+/Li for LTO (400). However, LTO (400) plateaus are less flat and have a steeper slope. The tails of the potential curves show dissimilar behavior. LTO (400) reveals a less steep decline above and below the plateau, matching the observation in the CV measurements.

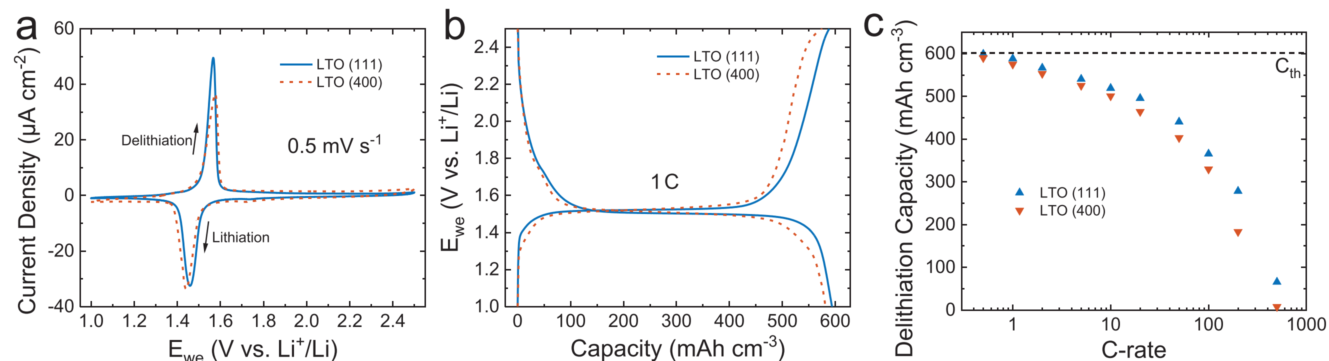

Figure 4. Comparison of electrochemical properties of strong (111)- and weak (400)-textured 30 nm $Li_4Ti_5O_{12}$ films. a) CV curves at 0.5 mV s^{-1}, b) second Galvanostatic cycle at 1 C, c) C-rate performance of the delithiation capacity from 0.5 C to 500 C.

© 2021 The Authors. Small published by Wiley-VCH GmbH

The delithiation capacity of LTO (111) (30 nm, 1 C) is in the same range as values reported for sputtered $Li_4Ti_5O_{12}$ films showing 565 (200 nm, 1 C) and 546 mAh cm^{-3} (100 nm, 0.5 C).[26,27] The galvanostatic profiles were either not reported[27] or with a similar of ratio bulk capacity, extracted from the plateau length, of around 80%.[26] Pagani et al. reported lower capacities and higher surface capacity contribution at low rates for a 110 nm film.[34] 20 nm epitaxial films probed by Hirayama et al. exhibited delithiation capacities of 720 and 550 mAh cm^{-3} with bulk capacity ratios of around 55 and 25% for (111) and (110) films, respectively. Cunha et al. highlighted the significant role of surface contribution in their study with a total capacity of around 1000 mAh cm^{-3}, but with a low bulk ratio of 40% at 3 C in the range of 1 to 2.5 V versus Li^+/Li.[25] The here reported ALD film has one of the highest bulk contributions with at least 80%, comparable to three times thicker films. The large variation of surface contribution highlights the need for a more standardized reporting for nanostructured $Li_4Ti_5O_{12}$ in the scientific community.

In the previous section, we concluded, based on previous studies, that surface storage contribution is probably causing the non-plateau capacity of the fully crystallized samples.[25,48] The contribution of the solid-electrolyte-interphase (SEI) layer to this reversible surface lithiation process is still under debate.[25,50] Scan rate-dependent diagnosis in cyclic voltammetry was proven unsuitable, especially for $Li_4Ti_5O_{12}$, to distinguish between diffusion-controlled intercalation (bulk) and pseudocapacitive storage (surface).[51] However, Cunha et al. demonstrated that the bulk capacity can be sufficiently differentiated by only taking the plateau into account.[25] The additional surface capacity is less pronounced for $Li_4Ti_5O_{12}$ in combination with solid electrolytes compared to liquid electrolytes.[27] Hence, maximizing the ratio of bulk capacity is of high importance for solid-state TFB applications. Ganapathy et al. calculated that lithium storage is allowed at lower energies corresponding to higher voltages for specific surfaces.[48] (100) surface facets are energetically most favorable for Li-ion insertion. However, (111) and (110) surface facets also allow Li insertion at voltages above the plateau. Furthermore, additional storage at (111) surface facets below the bulk voltage plateau exceeding the bulk $Li_7Ti_5O_{12}$ composition was discovered.[48] The higher ratio of surface to bulk for nanostructured particles or films explains the observed potential curves with enhanced surface contribution and capacities partially exceeding the theoretical value in nanostructured $Li_4Ti_5O_{12}$.[19,20,22,52] Cunha et al. demonstrated the effect of surface storage for epitaxial $Li_4Ti_5O_{12}$ films in various orientations.[25] They found that (100) orientation with the highest amount of (111) surface facets results in the largest additional capacity, visible in the tails of the potential curve. As mentioned earlier, the 55 nm films studied by Cunha et al. exhibit significantly larger surface storage contribution compared to the here presented films, with only half the film thickness. One explanation could be the higher surface roughness and a larger amount of (111) surface facets of the epitaxial film with (100) orientation synthesized by pulsed laser deposition (PLD) in contrast to the ALD films.[25]

It should be noted that an epitaxial orientation is not the same as a texture in polycrystalline films. The surface facets have a higher variation even in highly textured polycrystalline films. However, the basic principle of surface orientation-dependent additional Li-ion storage could explain the difference in the potential curves of the presented LTO (111) and LTO (400) films. Higher surface roughness or a different ratio of surface facets could explain the higher amount of non-plateau capacity of the (400)-textured film. The larger bulk capacity for LTO (111) could result in superior rate performance, which will be investigated next.

Figure 4c demonstrates the excellent C-rate performance of both samples. LTO (111) shows even superior delithiation capacities obtained at C-rates up to 500 C. This is remarkable since the films were exposed to air after deposition and crystallization, causing surface contaminations. From 0.5 C to 10 C, the values are quite similar with capacity declines from 599 to 519 mAh cm^{-3} and 590 to 501 mAh cm^{-3} for LTO (111) and LTO (400), respectively. The spreading increases drastically with up to 35% lower values for LTO (400) at higher C-rates. An outstanding discharge capacity of 440 mAh cm^{-3} at 50 C is demonstrated for LTO (111). Even at extreme rates of 200 C, this film reaches almost 50 % of C_{th} with 278 mAh cm^{-3}. The capacity dropped to around 11% of C_{th} for 500 C. This sharp decline could also be related to limitations of the applied cell design.

Both types of textured films show an excellent rate performance. The film thickness of only 30 nm enhances the Li-ion diffusion, which is the main limiting factor for high C-rates in $Li_4Ti_5O_{12}$ thin films.[25] Besides the nanostructuring, other effects have to play an essential role in explaining the different high-rate behavior of both samples. We identify that the type and degree of the film texture are crucial for the superior performance of LTO (111). The higher amount of surface contribution in lithium storage of LTO (400) is a clear disadvantage at higher currents due to the kinetic limitation of this storage mechanism at higher C-rates, which will be discussed in more detail in the next section. The strong texture of LTO (111) leads to highly parallel oriented grains in the polycrystalline film. This affects the kinetic of Li-ion transport within the film. Cunha et al. showed that instead of a strict one-dimension lithiation front parallel to the film, lithiation occurs along the grain boundaries and inserts radial into the grains.[25] Hence, the highly oriented grains and grain boundaries resulting in shorter diffusion pathways could lead to superior C-rate performance. The texture has an inferior effect on the bulk capacity due to the 3D Li-ion diffusion pathways in spinel $Li_4Ti_5O_{12}$.[21] Another factor could be the differences in lattice mismatch and resulting strain described in the previous section. The compressive strain of LTO (400)-textured samples is linked to increased Li-ion transport energy barriers and changes in the electronic structure.[27] Minor effects could be attributed to the higher amount of $Ti_xO_yN_z$ at the surface and lower specific resistivity of pCVD TiN, hampering the electron transport from the current collector to the $Li_4Ti_5O_{12}$ anode at high currents.[36] Smaller grains would also be beneficial for the C-rate performance.[53] However, the significant in-plane crystallite size was not quantifiable.

2.4. High-Power and Long-Cycle Life of ALD $Li_4Ti_5O_{12}$ (111)-Textured Films

In the previous section, we demonstrated that nanostructured 30 nm ALD $Li_4Ti_5O_{12}$ films have an excellent high-rate capability

© 2021 The Authors. Small published by Wiley-VCH GmbH

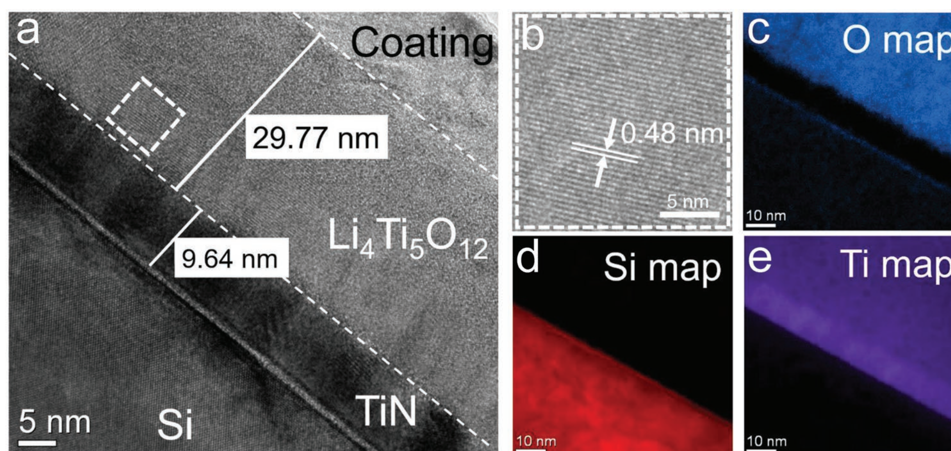

Figure 5. a) TEM micrograph of a layer stack consisting of 30 nm $Li_4Ti_5O_{12}$ and 10 nm ALD TiN after annealing. (b) High-resolution TEM of ALD $Li_4Ti_5O_{12}$ with a lattice spacing of 0.48 nm. EFTEM elemental maps of (c), O (d) Si, and (e) Ti.

as thin-film battery anodes. Strong (111)-textured films showed even superior performance at extreme rates above 50 C compared to layers with a preferred (400) growth direction. Next, we will discuss an in-depth view of the high-power capability and the cycle life at high rates of LTO (111) resulting from a high-quality layer stack.

The transmission electron microscopy (TEM) micrographs and energy-filtered TEM (EFTEM) elemental maps in **Figure 5** show the interface of spinel $Li_4Ti_5O_{12}$ and TiN after annealing and previous to electrochemical measurements. A smooth interface without elemental mixing is crucial for fast electron transport and stable Li-ion insertion/extraction for long-cycle life at high rates. Figure 5a illustrates that the layer stack is undamaged, and the ALD $Li_4Ti_5O_{12}$ reveals excellent adhesion, layer quality, and sharp interfaces. The high-resolution TEM micrograph of the enlarged dashed area in Figure 5b shows high crystallinity with an interlayer spacing of around 0.48 nm, indicating $Li_4Ti_5O_{12}$ (111). The EFTEM elemental maps in Figure 5c–e emphasize the observed sharp interfaces from TEM. It should be noted that it was not possible to detect Li with the applied EFTEM technique. No interface mixing of $Li_4Ti_5O_{12}$ and TiN is visible since the O signal shows a sharp interface towards the TiN. The small line of O between the Si substrate and the TiN film corresponds to the native SiO_2. The Ti map in Figure 5e shows higher intensity within the TiN. This is according to the lower Ti amount in $Li_4Ti_5O_{12}$. Detailed high-temperature Li-ion blocking capability of the applied 10 nm ALD TiN film was demonstrated in a previous study.[36]

The extreme high-power performance and ultra-long cycle life at high rates of ALD $Li_4Ti_5O_{12}$ with a strong (111)-texture is illustrated in **Figure 6**. CV measurements with scan rates from 0.5 to 10 mV s^{-1} are shown in Figure 6a. The lithiation and delithiation peaks are located at 1.45 and 1.59 V versus Li^+/Li (1 mV s^{-1}), 1.37 and 1.66 V versus Li^+/Li (5 mV s^{-1}), 1.30 and 1.72 V versus Li^+/Li (10 mV s^{-1}), respectively. The peak splitting demonstrates a linear dependency on the scan rate with an increase from 0.11 V for 0.5 mV s^{-1} to 0.42 V for 10 mV s^{-1}. The delithiation peaks are sharper and have higher peak current densities for all scan rates. The lithiation peaks are broadened, especially for increased scan rates, indicating higher lithiation resistance. Figure 6b illustrates the potential curves of the GCPLs of the various C-rates. The excellent delithiation capacity dependency on the C-rate was already discussed in Figure 4c in the previous section. The measured capacities for lithiation and delithiation match very well, indicating high Coulomb efficiency. In general, the higher lithiation capacities are due to a small increase in the SEI layer thickness and subsequent dissolving into the liquid electrolyte during delithiation, especially pronounced for nanosized films.[25,50] The difference in the shape of the curves is rather small up to 10 C. The splitting of the flat potential plateaus increases with higher C-rates. However, the slopes of the plateaus are still small. It should be noted that the ratio of the tail capacity decreases with higher C-rates indicating that the additional surface storage mechanism is less prominent for high currents and thus kinetically limited. This is in contrast to a rather constant surface contribution over the range of 3 C to 30 C probed by Cunha et al. From 20 C to 200 C, the lithiation curves drop to lower voltages and show broader plateaus. The delithiation curves still demonstrate large plateau capacities and smaller overpotentials, indicating lower delithiation resistance. This is according to the CV results. The large delithiation plateaus demonstrate that the dominant storage process at high rates is intercalation into the bulk of the film. At 500 C, the accessible capacities drop drastically, and the potential curves in both directions do not show plateaus indicating a higher contribution of surface storage.

A closer look at the Coulomb efficiency is shown in Figure 6c. GCPL from 0.5 C to 500 C with 10 cycles at each C-rate was performed. In the end, 10 cycles at 2 C were executed to investigate possible irreversible capacity losses. It should be noted that the capacity is normalized to the footprint area to demonstrate the accessible capacities as a planar TFB. The values were converted by multiplying the volumetric capacities with the film thickness of 30 nm. The maximum theoretical footprint capacity of this sample is 1.8 µAh cm^{-2}. The C-rate performance is according to the behavior shown in Figure 6b. Overall the Coulomb efficiency is excellent. In the beginning, at low C-rates, only around 99% are reached. This could indicate that interface formation processes still occur or less reversible reaction is caused by the surface storage mechanism of $Li_4Ti_5O_{12}$

© 2021 The Authors. Small published by Wiley-VCH GmbH

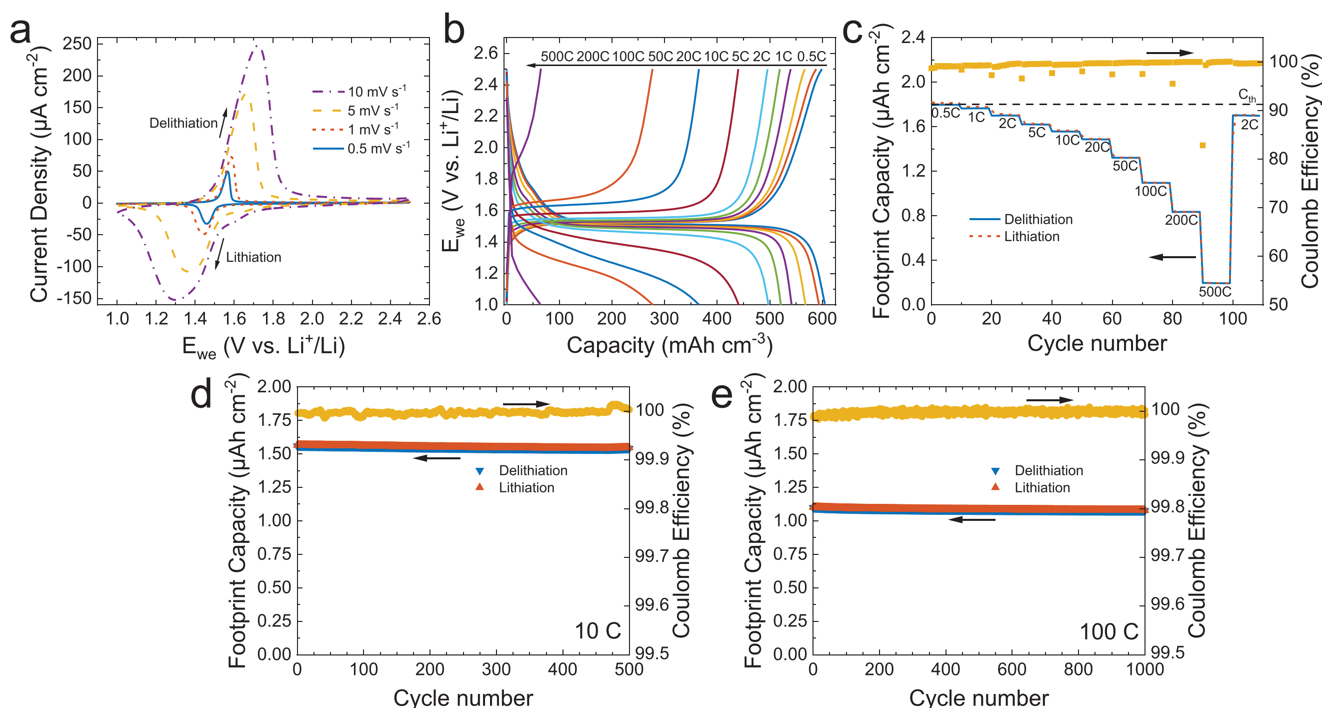

Figure 6. High-power and cycle life properties of ALD (111)-textured $Li_4Ti_5O_{12}$ thin films. a) CV with scan rates from 0.5 to 10 mV s^{-1}. b) Voltage profiles of Galvanostatic cycling at C-rates from 0.5 C to 500 C. c) Footprint capacity and Coulomb efficiency for the rate performance with 10 cycles at each C-rate. Footprint capacity and Coulomb efficiency for d) 500 cycles at 10 C and for e) 1000 cycles at 100 C.

discussed previously. The Coulomb efficiency increases above 99.99% at high C-rates, demonstrating that the bulk storage mechanism is highly reversible. The obtained footprint capacity at 2 C of 1.70 µAh cm^{-2} at the end of the procedure is 99.7% of the starting value. This is another proof that the high current densities of up to 0.9 mA cm^{-2} (500 C) do not damage the high-quality ALD $Li_4Ti_5O_{12}$ film.

The outstanding cycle stability at high rates of 10 C and 100 C of the ALD $Li_4Ti_5O_{12}$ is shown in Figure 6d,e. The high C-rates were chosen to investigate cycle life for targeted high-power applications. At 10 C, an initial footprint capacity of around 1.56 µAh cm^{-2} is accessible. Excellent Coulomb efficiency of above 99.997% and capacity retention of 98.8% of the initial capacity after 500 cycles is reached. Even at an extreme rate of 100 C, the Coulomb efficiency is above 99.996%. Exceptional 97.9% of the initial 1.10 µAh cm^{-2} are achieved after 1000 cycles. Figure S4 in the Supporting Information demonstrates that the potential profiles after 500 (10 C) and 1000 cycles (100 C) are highly similar to the initial curves. This indicates stable SEI and surface reconstruction leading to a highly reversible Li-ion insertion mechanism. Due to the low volume expansion upon lithiation, $Li_4Ti_5O_{12}$ is a well-known material with a long-cycle life.[22] Around 99.5% capacity retention after 2000 cycles at 50 C was demonstrated for $Li_4Ti_5O_{12}$ nanosheet-based hierarchical microspheres applied in an electrode slurry paste.[19] However, this performance is more challenging for thin films due to typical issues like contact loss to the current collector and material degradation. For example, sputtered thin films showed 6% capacity loss after 500 cycles at a low rate of 1 C.[47] The remarkable ultra-long cycle life at high C-rates and thus low material degradation of ALD $Li_4Ti_5O_{12}$ is based on excellent uniformity, high-quality interfaces, and superb adhesion of the film.

2.5. Benchmarking of $Li_4Ti_5O_{12}$ Thin Films

In this section, the excellent C-rate performance of ALD $Li_4Ti_5O_{12}$ with a strong (111)-texture will be benchmarked against other planar $Li_4Ti_5O_{12}$ thin films. For the first time in literature, $Li_4Ti_5O_{12}$ by ALD was electrochemically evaluated in this study. Hence, it will be compared with the C-rate performance of selected publications of $Li_4Ti_5O_{12}$ thin films deposited via various techniques. The most common method is the PVD-based sputtering process.[26,27,34,47] Other techniques chosen here are PLD[25,46] and metal-organic chemical vapor deposition (MOCVD).[54] 54 nm $Li_4Ti_5O_{12}$ thin films synthesized by a solid-state reaction (SSR) of oxidized Ti and Li_2CO_3 are additionally chosen for C-rate comparison with a more similar thickness.[55] Furthermore, the feasibility of the deposition techniques for high-energy 3D TFBs and high-volume production will be discussed.

Figure 7 demonstrates the superior high-rate performance of the ALD $Li_4Ti_5O_{12}$ film compared to all other deposition techniques. It should be noted that benchmarking, in general, can be affected by several other parameters. In this case, these are factors such as the applied voltage window, bulk to surface capacity ratio, cell design, electrolyte, surface area, current collector, and mechanical electrical contact. The illustration nevertheless could act as a useful orientation and a reference for further studies. The bulk capacity ratio of the here reported 30 nm ALD film is similar or even higher than films with

© 2021 The Authors. Small published by Wiley-VCH GmbH

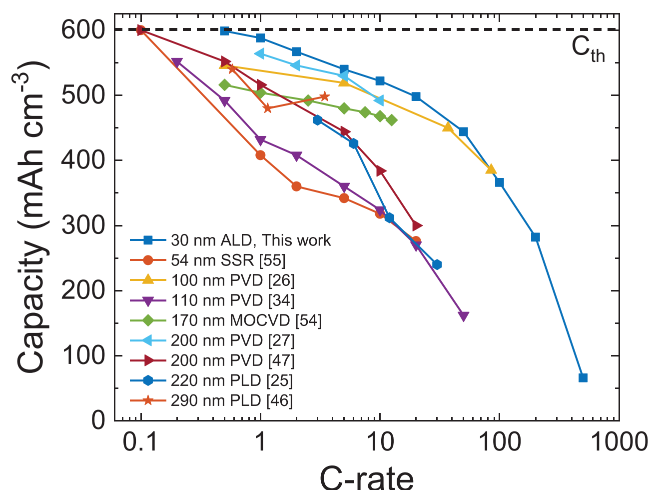

Figure 7. The comparison of the rate capability of ALD $Li_4Ti_5O_{12}$ with other $Li_4Ti_5O_{12}$ thin films fabricated by various deposition techniques in recently reported studies. The capacities were estimated based on their results of C-rate performance.

thicknesses of 100 nm and above, enabling a reasonable comparison.[25–27,34,46,47,54] In general, the benefit of scaling the film thickness is visible in Figure 7. Film thicknesses below 200 nm can compensate the low ionic and electronic conductivity of $Li_4Ti_5O_{12}$. Nanostructuring is a well-known optimization parameter.[19,22] The here introduced 30 nm ALD film offers the shortest Li-ion diffusion pathways. However, the film with the most similar thickness of 54 nm by Labyedh et al. showed low capacities at higher C-rates, which could be due to impurity issues with the solid-state reaction or the platinum current collector.[55] Overall, the ALD film shows one of the highest accessible capacities close to the theoretical maximum at moderate rates around 1 C. The majority of the data was just reported for C-rates below 20 C, hampering high-power comparability. Wunde et al. showed competitive data up to around 100 C.[26] However, in their study and most of the literature data of $Li_4Ti_5O_{12}$ thin films, long cycle life behavior was not reported.

Another parameter for the superior high-rate performance of the ALD film could be the electron transport at the interface towards the current collector. Most studies used Pt, which is a standard material for investigations in the lab scale.[27,34,46,47,54] However, the work function of TiN has a better overlap with the conduction band of $Li_4Ti_5O_{12}$ compared to Pt resulting in superior electrical transport.[55] Furthermore, TiN is an ideal, established, and cost-effective current collector for TFB production beyond lab scale.[36]

All compared methods suffer from a low areal capacity due to the limited film thickness, especially for ALD. In general, for compensation of the low energy density of TFBs, high aspect ratio substrates enabling 3D TFBs could be applied.[8] Conformal coating of these structures is not possible with PVD-based processes. Even MOCVD only showed suitability for aspect ratios below 10.[54] On the other hand, ALD is an ideal technique to enable aspect ratios of 50 and above, compensating for the lower film thickness compared to sputtered layers.[10] The capabilities of ALD $Li_4Ti_5O_{12}$ for 3D TFBs will be investigated in future studies. Furthermore, ALD has the highest potential of all compared methods for upscaling to high volume production of 3D TFB via utilization of established 300 mm Si technology or roll-to-roll spatial ALD.[7,16,17,32,56]

3. Conclusion

In this study, highly-textured spinel $Li_4Ti_5O_{12}$ thin films fabricated by ALD have been electrochemically probed for the first time, demonstrating excellent high-power performance and ultra-long cycle life at high rates. The developed thermal ALD process with LiHMDS precursor and a growth per cycle of 0.6 Å cycle^{-1} at 300 °C enables high-quality films with smooth interfaces after post-deposition crystallization at 750 °C. The planar 30 nm $Li_4Ti_5O_{12}$ film reaches 98% of the theoretical capacity with 588 mAh cm^{-3} at 1 C. The undesired surface contribution to the capacity, typical for thin films, is minimized by an optimized crystallization process and significantly lower than reported values of $Li_4Ti_5O_{12}$ films below 100 nm. The limiting factor of slow Li-ion diffusion is compensated by nanostructuring with an ultrathin 30 nm film resulting in outstanding rate performance. The type and degree of film texture depend on the underlying substrate and influences the electrochemical properties. We identify a strong (111)-texture of $Li_4Ti_5O_{12}$ on ALD TiN as a key tuning parameter for the superior C-rate performance compared to a weak (400)-texture on pCVD TiN. The highly parallel grains of the (111)-textured $Li_4Ti_5O_{12}$ film enable discharge capacities of 278 mAh cm^{-3} at extreme rates of 200 C. Outstanding cycle performance due to a high Coulomb efficiency is demonstrated, resulting in 97.9% capacity retention after 1000 cycles of the initial 366 mAh cm^{-3} at 100 C. The superior performance of thin films by ALD compared to other deposition techniques and the capabilities for high-volume manufacturing make strong (111)-textured $Li_4Ti_5O_{12}$ a promising anode towards integrated 3D TFBs for autonomous IoT devices. Furthermore, these highly controllable ALD thin films enable model systems to gain in-depth insights into the advantageous effects of nanostructuring and nanoionics. This could pave the way for breakthroughs in nanoparticle-based liquid Li-ion batteries and large-scale solid-state batteries.

4. Experimental Section

$Li_4Ti_5O_{12}$ Film Preparation: ALD of $Li_4Ti_5O_{12}$ thin films was carried out in a FlexAl system (Oxford Instruments) on 200 mm Si wafers. LiHMDS (STREM Chemicals, 97%), TDMAT (STREM Chemicals, 99%), and H_2O were used. The LiHMDS and TDMAT precursors were kept at 70 and 60 °C, respectively. Both were applied via bubbling mode with Ar as the carrier gas in heated lines to avoid condensation. An ALD step consists of a precursor pulse and a subsequent purge sub-step. The pulse times of TDMAT and H_2O were kept at 0.5 and 0.25 s, respectively. During process development, the pulse times of LiHMDS were varied between 0 and 8 s. All purge sub-steps were carried out for 10 s to evacuate unreacted precursor. A three-step ALD process was applied to suppress the so-called "water reservoir effect" occurring due to the hygroscopic nature of the material.[32] The novel concept is the introduction of a co-precursor step B (here TDMAT) between the LiHMDS (A) and the H_2O (C) steps. Classic supercycle ALD processes consist of alternating subcycles with the basic order AC and BC. The substrate temperature was

© 2021 The Authors. Small published by Wiley-VCH GmbH

varied between 220 and 320 °C for investigation of the ALD temperature window. Process development was performed on 200 mm Si substrates with 100 nm thermal SiO_2. Samples for electrochemical characterization were deposited on p-type 300 mm Si (100) substrates with a resistivity of 0.013 Ohm cm coated with either 35 nm pCVD or 10 nm ALD TiN. The process conditions of the TiN depositions were reported previously.[36] Both TiN films were proven as excellent Li diffusion barriers and current collectors, however the ALD film demonstrated superior performance, especially in 3D structured substrates.[36] The crystallization of the post-deposition amorphous $Li_4Ti_5O_{12}$ films was conducted in an Solaris 75 rapid thermal processor (SSI) with Ar purging.

Structural Characterization: Phase and crystallization information was characterized by GI-XRD analysis on a D8 Discover system (Bruker). Experiments were carried out with Cu Kα radiation ($\lambda = 1.5406$ Å), 40 kV, and 40 mA at an incidence angle of 0.3° with a 2θ range of 10° to 90°. The step time and size were set at 10 s and 0.1°, if not otherwise noted. Phi was set at 45° to suppress peaks related to the Si substrate. The thickness and morphology of the samples were observed by SEM on a S-5000 system (Hitachi) and by iSE on a M2000X-210 (J.A. Woollam) in the wavelength range from 210 to 1000 nm and Xenon light source. TEM was performed with an electron beam energy of 200 keV on a Tecnai F20 XT (FEI). EFTEM using a imaging filter (Gatan) provided element-sensitive micrographs. Filter energies of 99, 456, and 532 eV were applied for Si, Ti, and O, respectively.

Electrochemical Measurements: A three-electrode setup was used for electrochemical measurements. 15 by 15 mm coupons of the $Li_4Ti_5O_{12}$ samples on TiN substrates were employed for electrochemical analysis. It should be noted that the samples were exposed to air after deposition and annealing, although it was kept to a minimum. TSC surface cells (rhd instruments) with an active area of 0.273 cm^2 were assembled in an argon-filled glovebox (Mbraun, H_2O and O_2 levels below 1 ppm). As electrolyte 1M lithium hexafluorophosphate ($LiPF_6$) in ethylene carbonate/diethyl carbonate (EC/DEC 1:1) (Sigma-Aldrich, battery grade) and as counter and reference electrodes Li stripes (Sigma-Aldrich, 99.9%) were applied. The sample was contacted via the bottom of the Si substrate. All electrochemical measurements were performed and analyzed with a SP-150 (Bio-Logic) and EC-Lab software. All potentials mentioned in this report were measured against Li^+/Li. The electrochemical measurements were performed in the potential range of 1 to 2.5 V versus Li^+/Li if not otherwise noted. Considering a maximum theoretical volumetric capacity of 600 mAh cm^{-3}, the applied currents of 0.9 to 900 µA cm^{-2} correlate to C-rates of 0.5 C to 500 C for a 30 nm film.

Supporting Information

Supporting Information is available from the Wiley Online Library or from the author.

Acknowledgements

This work was supported as a Fraunhofer LIGHTHOUSE PROJECT. Open access funding enabled and organized by Projekt DEAL.

Conflict of Interest

The authors declare no conflict of interest.

Data Availability Statement

The data that support the findings of this study are available from the corresponding author upon reasonable request.

Keywords

atomic layer deposition, fast charging, Li-ion batteries, lithium titanium oxide (LTO), thin films

Received: May 5, 2021
Revised: June 3, 2021
Published online: July 17, 2021

[1] Y. Khan, A. E. Ostfeld, C. M. Lochner, A. Pierre, A. C. Arias, *Adv. Mater*. **2016**, *28*, 4373.
[2] J. Mouly, *Wearables in Consumer and Medical Applications 2020. Report* **2020**.
[3] C. Chen, M. Jiang, T. Zhou, L. Raijmakers, E. Vezhlev, B. Wu, T. U. Schülli, D. L. Danilov, Y. Wei, R.-A. Eichel, P. H. L. Notten, *Adv. Energy Mater.* **2021**, *11*, 2003939.
[4] Y. Wang, B. Liu, Q. Li, S. Cartmell, S. Ferrara, Z. D. Deng, J. Xiao, *J. Power Sources* **2015**, *286*, 330.
[5] J. H. Pikul, H. Gang Zhang, J. Cho, P. V. Braun, W. P. King, *Nat. Commun.* **2013**, *4*, 1732.
[6] a) J. W. Long, B. Dunn, D. R. Rolison, H. S. White, *Chem. Rev.* **2004**, *104*, 4463; b) J. F. M. Oudenhoven, L. Baggetto, P. H. L. Notten, *Adv. Energy Mater.* **2011**, *1*, 10; c) S. Ferrari, M. Loveridge, S. D. Beattie, M. Jahn, R. J. Dashwood, R. Bhagat, *J. Power Sources* **2015**, *286*, 25; d) C. Yue, J. Li, L. Lin, *Front. Mech. Eng.* **2017**, *12*, 459.
[7] A. Pearse, T. Schmitt, E. Sahadeo, D. M. Stewart, A. Kozen, K. Gerasopoulos, A. A. Talin, S. B. Lee, G. W. Rubloff, K. E. Gregorczyk, *ACS Nano* **2018**, *12*, 4286.
[8] S. Moitzheim, B. Put, P. M. Vereecken, *Adv. Mater. Interfaces* **2019**, *28*, 1900805.
[9] a) N. P. Dasgupta, H.-B.-R. Lee, S. F. Bent, P. S. Weiss, *Chem. Mater.* **2016**, *28*, 1943; b) R. A. Ovanesyan, E. A. Filatova, S. D. Elliott, D. M. Hausmann, D. C. Smith, S. Agarwal, *J. Vac. Sci. Technol., A* **2019**, *37*, 60904.
[10] O. Nilsen, K. B. Gandrud, R. Amund, F. Helmer, *Atomic Layer Deposition in Energy Conversion Applications*, Wiley, Hoboken, NJ **2017**, p. 183.
[11] X. Meng, *Energy Storage Mater.* **2020**, *30*, 296.
[12] a) V. Miikkulainen, A. Ruud, E. Østreng, O. Nilsen, M. Laitinen, T. Sajavaara, H. Fjellvåg, *J. Phys. Chem. C* **2014**, *118*, 1258; b) R. Sheil, D. Butts, K. Jungjohann, J. Yoo, B. Dunn, J. P. Chang, *J. Vac. Sci. Technol., A* **2021**, *39*, 12408.
[13] M. E. Donders, W. M. Arnoldbik, H. C. M. , Knoops, W. M. M. Kessels, P. H. L. Notten, *J. Electrochem. Soc.* **2013**, *160*, A3066.
[14] a) B. Put, M. J. Mees, N. Hornsveld, S. Hollevoet, A. Sepúlveda, P. M. Vereecken, W. M. M. Kessels, M. Creatore, *J. Electrochem. Soc.* **2019**, *166*, A1239; b) A. C. Kozen, A. J. Pearse, C.-F. Lin, M. Noked, G. W. Rubloff, *Chem. Mater.* **2015**, *27*, 5324.
[15] Y.-C. Perng, J. Cho, S. Y. Sun, D. Membreno, N. Cirigliano, B. Dunn, J. P. Chang, *J. Mater. Chem. A* **2014**, *2*, 9566.
[16] S. Moitzheim, J. E. Balder, R. Ritasalo, S. Ek, P. Poodt, S. Unnikrishnan, S. de Gendt, P. M. Vereecken, *ACS Appl. Energy Mater.* **2019**.
[17] S. Moitzheim, J. E. Balder, P. Poodt, S. Unnikrishnan, S. de Gendt, P. M. Vereecken, *Chem. Mater.* **2017**, *29*, 10007.
[18] S. Scharner, W. Weppner, P. Schmid-Beurmann, *J. Electrochem. Soc.* **1999**, *146*, 857.
[19] D. Wang, H. Liu, M. Li, X. Wang, S. Bai, Y. Shi, J. Tian, Z. Shan, Y. S. Meng, P. Liu, et al., *Energy Storage Mater.* **2019**, *21*, 361.
[20] Y. He, A. Muhetaer, J. Li, F. Wang, C. Liu, Q. Li, D. Xu, *Adv. Energy Mater.* **2017**, *7*, 1700950.
[21] Y. Zhu, J. C. Gonzalez-Rosillo, M. Balaish, Z. D. Hood, K. J. Kim, J. L. M. Rupp, *Nat. Rev. Mater.* **2020**, *6*, 313.

© 2021 The Authors. Small published by Wiley-VCH GmbH

[22] B. Zhao, R. Ran, M. Liu, Z. Shao, *Mater. Sci. Eng., R* **2015**, *98*, 1.
[23] T. Yuan, Z. Tan, C. Ma, J. Yang, Z.-F. Ma, S. Zheng, *Adv. Energy Mater.* **2017**, *7*, 1601625.
[24] W. Zhang, D.-H. Seo, T. Chen, L. Wu, M. Topsakal, Y. Zhu, D. Lu, G. Ceder, F. Wang, *Science* **2020**, *367*, 1030.
[25] D. M. Cunha, T. A. Hendriks, A. Vasileiadis, C. M. Vos, T. Verhallen, D. P. Singh, M. Wagemaker, M. Huijben, *ACS Appl. Energy Mater.* **2019**, *2*, 3410.
[26] F. Wunde, F. Berkemeier, G. Schmitz, *J. Power Sources* **2012**, *215*, 109.
[27] A. Sepúlveda, J. Speulmanns, P. M. Vereecken, *Sci. Technol. Adv. Mater.* **2018**, *19*, 454.
[28] R. Pfenninger, S. Afyon, I. Garbayo, M. Struzik, J. L. M. Rupp, *Adv. Funct. Mater.* **2018**, *28*, 1800879.
[29] V. Miikkulainen, O. Nilsen, M. Laitinen, T. Sajavaara, H. Fjellvåg, *RSC Adv.* **2013**, *3*, 7537.
[30] X. Meng, J. Liu, X. Li, M. N. Banis, J. Yang, R. Li, X. Sun, *RSC Adv.* **2013**, *3*, 7285.
[31] V. Miikkulainen, M. Leskelä, M. Ritala, R. L. Puurunen, *J. Appl. Phys.* **2013**, *113*, 021301.
[32] S. Bönhardt, K. Kühnel, A. M. Kia, W. Weinreich, *J. Vac. Sci. Technol., A* **2019**, *37*, 31508.
[33] A. Werbrouck, F. Mattelaer, M. Minjauw, M. Nisula, J. Julin, F. Munnik, J. Dendooven, C. Detavernier, *J. Phys. Chem. C* **2020**, *124*, 27829.
[34] F. Pagani, M. Döbeli, C. Battaglia, *Batteries Supercaps* **2021**, *4*, 316.
[35] A. C. Kozen, A. J. Pearse, C.-F. Lin, M. A. Schroeder, M. Noked, S. B. Lee, G. W. Rubloff, *J. Phys. Chem. C* **2014**, *118*, 27749.
[36] J. Speulmanns, A. M. Kia, K. Kühnel, S. Bönhardt, W. Weinreich, *ACS Appl. Mater. Interfaces* **2020**, *12*, 39252.
[37] L. Baggetto, R. A. H. Niessen, F. Roozeboom, P. H. L. Notten, *Adv. Funct. Mater.* **2008**, *18*, 1057.
[38] A. M. Kia, S. Bönhardt, S. Zybell, K. Kühnel, N. Haufe, W. Weinreich, *Phys. Status Solidi A* **2019**, *5*, 1800769.
[39] M. Lederer, A. Reck, K. Mertens, R. Olivo, P. Bagul, A. Kia, B. Volkmann, T. Kämpfe, K. Seidel, L. M. Eng, *Appl. Phys. Lett.* **2021**, *118*, 012901.
[40] R. Methaapanon, S. F. Bent, *J. Phys. Chem. C* **2010**, *114*, 10498.
[41] W. Weinreich, L. Wilde, J. Müller, J. Sundqvist, E. Erben, J. Heitmann, M. Lemberger, A. J. Bauer, *J. Vac. Sci. Technol., A* **2013**, *31*, 01A119.
[42] a) U. Roy, K. Petrov, I. Tsolovski, P. Peshev, *Phys. Status Solidi A* **1977**, *44*, K25; b) Z. H. Cen, B. X. Xu, J. F. Hu, R. Ji, Y. T. Toh, K. D. Ye, Y. F. Hu, *J. Phys. D: Appl. Phys.* **2017**, *50*, 075105.
[43] W. Fang, C.-Y. Lo, *Sens. Actuators, A* **2000**, *84*, 310.
[44] a) L. Cai, M. Zou, H. Abu-Safe, H. Naseem, W. Brown, *J. Electron. Mater.* **2007**, *36*, 191; b) G. Abadias, E. Chason, J. Keckes, M. Sebastiani, G. B. Thompson, E. Barthel, G. L. Doll, C. E. Murray, C. H. Stoessel, L. Martinu, *J. Vac. Sci. Technol., A* **2018**, *36*, 020801.
[45] Z. Yu, G. Zhu, H. Xu, A. Yu, *Energy Technol.* **2014**, *2*, 767.
[46] J. Deng, Z. Lu, I. Belharouak, K. Amine, C. Y. Chung, *J. Power Sources* **2009**, *193*, 816.
[47] C.-F. Xiao, J. H. Kim, D. Choi, Y. C. Park, J. H. Kim, J. Park, Y. J. Kim, H.-S. Kim, *J. Alloys Compd.* **2019**, *801*, 550.
[48] S. Ganapathy, M. Wagemaker, *ACS Nano* **2012**, *6*, 8702.
[49] M. Hirayama, K. Kim, T. Toujigamori, W. Cho, R. Kanno, *Dalton Trans.* **2011**, *40*, 2882.
[50] M.-S. Song, R.-H. Kim, S.-W. Baek, K.-S. Lee, K. Park, A. Benayad, *J. Mater. Chem. A* **2014**, *2*, 631.
[51] a) M. Opitz, J. Yue, J. Wallauer, B. Smarsly, B. Roling, *Electrochim. Acta* **2015**, *168*, 125; b) C. Costentin, *J. Phys. Chem. Lett.* **2020**, *11*, 9846.
[52] a) G. B. Xu, W. Li, L. W. Yang, X. L. Wei, J. W. Ding, J. X. Zhong, P. K. Chu, *J. Power Sources* **2015**, *276*, 247; b) L. Y. Yang, H. Z. Li, J. Liu, S. S. Tang, Y. K. Lu, S. T. Li, J. Min, N. Yan, M. Lei, *J. Mater. Chem. A* **2015**, *3*, 24446.
[53] X. M. Wu, J. L. Liu, S. Chen, F. R. Mai, C. an Li, *J. Solid State Electrochem.* **2012**, *16*, 3855.
[54] J. Xie, P.-P. R. Harks, D. Li, L. H. Raijmakers, P. H. Notten, *Solid State Ionics* **2016**, *287*, 83.
[55] N. Labyedh, B. Put, A.-A. E. Mel, P. M. Vereecken, *J. Electrochem. Soc.* **2018**, *165*, B3184.
[56] M. Ameen, I. Beeker, L. Haverkate, B. Anothumakkool, F. Grob, D. Hermes, N. Huijssen, S. del Khandan, F. Roozeboom, S. Unnikrishnan, *ECS Meet. Abstracts* **2020**, *MA2020-02*, 1695.

© 2021 The Authors. Small published by Wiley-VCH GmbH